

# A Model for the Fast Blue Optical Transient AT2018Cow: Circumstellar Interaction of a Pulsational Pair-instability Supernova

SHING-CHI LEUNG,<sup>1,2</sup> SERGEI BLINNIKOV,<sup>1,3,4</sup> KEN'ICHI NOMOTO,<sup>1</sup> PETR BAKLANOV,<sup>3,5,6</sup> ELENA SOROKINA,<sup>3,7</sup> AND  
ALEXEY TOLSTOV<sup>1,8</sup>

<sup>1</sup>*Kavli Institute for the Physics and Mathematics of the Universe (WPI), The University of Tokyo Institutes for Advanced Study, The University of Tokyo, Kashiwa, Chiba 277-8583, Japan*

<sup>2</sup>*TAPIR, Walter Burke Institute for Theoretical Physics, Mailcode 350-17, Caltech, Pasadena, CA 91125, USA*

<sup>3</sup>*National Research Center "Kurchatov institute," Institute for Theoretical and Experimental Physics (ITEP), 117218 Moscow, Russia*

<sup>4</sup>*Dukhov Automatics Research Institute (VNIIA), Suschevskaya 22, 127055 Moscow, Russia*

<sup>5</sup>*National Research Nuclear University MEPhI, Kashirskoe sh. 31, Moscow 115409, Russia*

<sup>6</sup>*Space Research Institute (IKI), Russian Academy of Sciences, Profsoyuznaya 84/32, 117997 Moscow, Russia*

<sup>7</sup>*Sternberg Astronomical Institute, M.V. Lomonosov Moscow State University, Universitetski pr. 13, 119234 Moscow, Russia*

<sup>8</sup>*The Open University of Japan, 2-11, Wakaba, Mihama-ku, Chiba, Chiba 261-8586, Japan*

(Dated: March 16, 2021; Received 7 February 2020; Accepted 18 September 2020; Published 3 November 2020)

## ABSTRACT

The Fast Blue Optical Transient (FBOT) ATLAS18qqn (AT2018cow) has a light curve as bright as superluminous supernovae but rises and falls much faster. We model this light curve by circumstellar interaction of a pulsational pair-instability (PPI) supernova (SN) model based on our PPISN models studied in previous work. We focus on the  $42 M_{\odot}$  He star (core of a  $80 M_{\odot}$  star) which has circumstellar matter of mass  $0.50 M_{\odot}$ . With the parameterized mass cut and the kinetic energy of explosion  $E$ , we perform hydrodynamical calculations of nucleosynthesis and optical light curves of PPISN models. The optical light curve of the first  $\sim 20$  days of AT2018cow is well-reproduced by the shock heating of circumstellar matter for the  $42 M_{\odot}$  He star with  $E = 5 \times 10^{51}$  erg. After day 20, the light curve is reproduced by the radioactive decay of  $0.6 M_{\odot}$   $^{56}\text{Co}$ , which is a decay product of  $^{56}\text{Ni}$  in the explosion. We also examine how the light curve shape depends on the various model parameters, such as CSM structure and composition. We also discuss (1) other possible energy sources and their constraints, (2) origin of observed high-energy radiation, and (3) how our result depends on the radiative transfer codes. Based on our successful model for AT2018cow and the model for SLSN with the CSM mass as large as  $20 M_{\odot}$ , we propose the working hypothesis that PPISN produces SLSNe if CSM is massive enough and FBOTs if CSM is less than  $\sim 1 M_{\odot}$ .

*Keywords:* Supernovae(1668) – Supernova dynamics(1664) – Concept: Radiative transfer – Concept: Light curves – Stellar pulsations(1625)

## 1. INTRODUCTION

The Fast Blue Optical Transient (FBOT) ATLAS18qqn/AT2018cow (COW) (Prentice et al. 2018; Perley et al. 2019) has a peak luminosity of  $1.7 \times 10^{44}$  erg  $\text{s}^{-1}$ , being as high as superluminous supernovae (SLSNe) (e.g., Gal-Yam 2012). But it shows a much faster evolution in its optical properties than SLSNe. Its brightness

rises five magnitudes within the first three days and also falls much faster than SLSNe. It shows hot blackbody spectra with an effective temperature  $\sim 27000$  K, which drops by  $\sim 12000$  K in two weeks. Its spectra are featureless without metal lines in both optical and UV, but show a quasi-static He feature (Kuin et al. 2019; Bietenholz et al. 2020). The detection of early X-ray and  $\gamma$ -ray indicates the possibility of having an inner energy source (e.g., Margutti et al. 2019).

Several models for the optical light curve of AT2018cow have been suggested, including the magnetar (e.g., Fang et al. 2019), electron capture super-

nova from an accretion-induced collapse of an ONeMg white dwarf<sup>1</sup> (Lyutikov & Toonen 2019), and circumstellar interaction model (e.g., Fox & Smith 2019). The circumstellar interaction model has been applied to one of FBOT, KSN 2015K, and successfully reproduces the short timescale of rise and decline (Rest et al. 2018; Tolstov et al. 2019). In particular, Tolstov et al. (2019) adopted the electron capture supernova model of a super-AGB star, which has an optically thick CSM with the mass of as small as  $\sim 0.1 M_{\odot}$ .

As an alternative to the supernova model, a tidal disruption event (TDE) has been proposed as a model for AT2018cow. See Perley et al. (2019); Liu et al. (2018); Kuin et al. (2019) for details. TDE is capable of reproducing the general  $t^{-5/3}$  dependence in supernova light curve (Goicovic et al. 2019), but it depends on the exact orbits around the massive black hole. For close encounter, the strong tidal force can trigger spontaneous nuclear runaway and explosion (Tanikawa 2018a,b).

In the present work, we consider the circumstellar interaction of the pulsational pair-instability (PPI) supernova (SN). It has been shown that stars as massive as initially  $80\text{--}140 M_{\odot}$  undergo PPI during O-burning because of the electron-positron pair creation (e.g., Barkat et al. 1967; Heger & Woosley 2002; Ohkubo et al. 2009; Yoshida et al. 2014; Woosley 2017; Marchant et al. 2019; Leung et al. 2019). Woosley et al. (2007) calculated the sequence of pulsational mass ejection of H-rich materials and interaction between the ejecta during the pulsation. Then they tried to reproduce the light curve of a Type II SLSN (SLSN-II) 2006.

In Leung et al. (2019), we have calculated the evolution of  $80 - 120 M_{\odot}$  stars with the metallicities of  $Z = 10^{-3} - 1.0 Z_{\odot}$  through the beginning of PPI. Assuming H-rich envelope is lost, we have further evolved their He cores of  $40 - 62 M_{\odot}$  with  $Z = 0$  through the core-collapse. During the pulsation, these He stars undergo extensive mass loss. The ejected masses are  $3 - 13 M_{\odot}$  for  $40 - 62 M_{\odot}$  He stars, as seen in Figure 1, because the pulsations are stronger for more massive He stars (see also Yoshida et al. 2014; Woosley 2017; Marchant et al. 2019). The ejecta form He-rich CSM.

The lack of metal lines in the spectra of AT2018cow suggests that the ejecta contains mostly He (Prentice et al. 2018). This feature is consistent with the PPISN model which ejects mostly the outer layer of the He star during pulsation. (The exact composition can be affected by other stellar parameters such as the

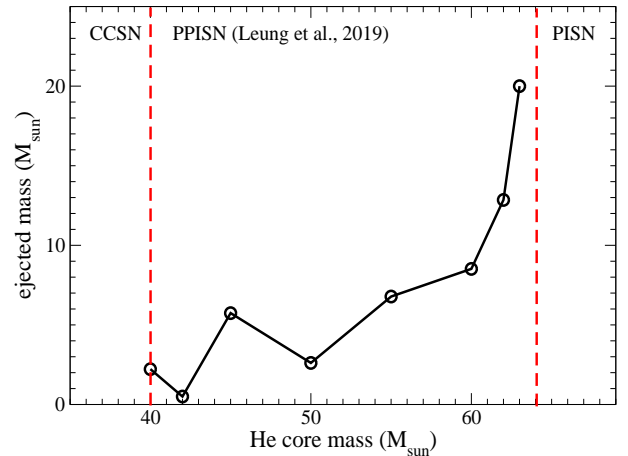


**Figure 1.** Total ejecta mass by pulsation against progenitor He core mass.

progenitor mass and rotation (Chatzopoulos & Wheeler 2012).)

Tolstov et al. (2017) applied a PPISN model of  $50 M_{\odot}$  He star (which is a He core of  $100 M_{\odot}$  star) with a large amount of an optically thick CSM ( $\sim 20 M_{\odot}$ ) and the kinetic energy of explosion as high as  $\sim 10^{52}$  erg  $\text{s}^{-1}$ . They calculated the circumstellar interaction and the resultant light curve. The model well-explains the light curve of Type I SLSN (SLSN-I) PTF 12dam, whose early curve shows a rise of 2.5 mag in 20 days. Such massive CSM is good to reproduce the slow rise of SLSN-I (see also Sorokina et al. 2016), but too massive to explain the fast rise of the light curve of AT2018cow (5 mag in 5 days).

Perley et al. (2019) have suggested that in order to reproduce the light curve qualitatively of AT2018cow, there is a pre-explosion ejected mass of  $\sim 0.5 M_{\odot}$ . We thus look for in Figure 1 the pulsational pair-instability supernova model which produces a similar CSM mass. We find that this corresponds to the He star model with the mass  $M_{\text{He}} = 42 M_{\odot}$ . This He star ejects  $0.50 M_{\odot}$  of its surface matter, composed of only He, to the surrounding at  $\sim 1.6$  year prior to its final collapse.

As seen from the models for SLSN (Tolstov et al. 2017) and FBOT (Tolstov et al. 2019), the mass of the optically thick CSM seems to determine the rising timescale of light curves. Based on this, we set here the following working hypothesis that PPISN produces SLSNe if CSM is massive enough and FBOTs if CSM is less than  $\sim 1 M_{\odot}$ .

Based on our working hypothesis, we perform the hydrodynamical simulations of the PPISN explosion of the  $42 M_{\odot}$  He star. We assume that the He star undergoes core collapse to form a black hole and generates an explosion. With the parameterized explosion energy,

<sup>1</sup> See Nomoto (1984); Nomoto & Kondo (1991); Zha et al. (2019); Leung et al. (2020) for details of the electron capture supernova model.

we calculate nucleosynthesis, circumstellar interaction, and bolometric light curves. From the comparison with the observed light curve of AT2018cow, we obtain the constraints on the explosion energy, mixing of radioactive  $^{56}\text{Ni}$ , density distribution of CSM, and some other model parameters.

We note that radio and X-ray observations (Margutti et al. 2019) have provided hints that aspherical explosion is necessary for the peculiar evolution of this object. In this work, we use the one-dimensional simulation with spherical approximation as an exploratory work to see which parameters are necessary for reproducing the light curve of this object. We aim for fitting the global features of this light curve.

In Sections 2 and 3.1 we review the numerical scheme to calculate nucleosynthesis and the bolometric light curve.

In Section 4 we describe our optimized model which has a bolometric light curve closet to AT2018cow. We present the detailed evolution of the hydrodynamics and radiative transfer after its explosion.

In Section 5 we present a detailed numerical study to examine the sensitivity of our results on the model parameter and input physics. This includes the explosion energy,  $^{56}\text{Ni}$  distribution, and CSM properties.

In Section 6 we further discuss how other central energy sources can contribute or supplement to the light curve of AT2018cow. We also discuss how such central energy sources contribute produce to the high-energy photons and compare with AT2018cow. In the end, we show how our results depend on the radiative transfer code.

## 2. INITIAL MODEL AND METHODS OF HYDRODYNAMICAL SIMULATIONS

### 2.1. Presupernova Model

As discussed in Introduction, we adopt the  $42 M_{\odot}$  He star model which was evolved from the He main-sequence to the Fe core collapse by Leung et al. (2019) through PPI and associated mass ejection. We used the code MESA (Modules for the Experiments in Stellar Astrophysics) (Paxton et al. 2011, 2013, 2015, 2017) (Version 8118).

In Figure 2 we plot the pre-explosion configurations for the density and temperature (top left panel), velocity (top right panel), electron mole fraction  $Y_e$  (bottom left panel), and the chemical abundance (bottom right panel) against  $M(r)$ , where  $M(r)$  is the included mass within the radius  $r$ . Because the He star has lost  $0.50 M_{\odot}$  during PPI, the mass of the collapsing He star is  $41.50 M_{\odot}$ .

The chemical abundance profile shows three layers. The inner core at  $M(r) < 2M_{\odot}$ , which collapses to a proto-neutron star (and later a black hole), is made of mostly  $^{56}\text{Fe}$ . A small fraction of  $^4\text{He}$  exists due to the photo-disintegration. A trace of electron capture products, represented by  $^{56}\text{Cr}$ <sup>2</sup>, exist in the core, being insignificant at  $M(r) > 1 M_{\odot}$ . The envelope includes an inner envelope and an outer envelope which differ by their compositions. The inner envelope at  $M(r) = 2 - 8 M_{\odot}$  consists of mostly intermediate mass elements, featured by  $^{28}\text{Si}$  and  $^{32}\text{S}$ , and smaller amounts of  $^{36}\text{Ar}$  and  $^{40}\text{Ca}$ . In the outer envelope at  $M(r) = 8 - 35 M_{\odot}$ ,  $^{16}\text{O}$  dominates the composition, with a trace amount of  $^{20}\text{Ne}$  and  $^{24}\text{Mg}$ . The transition to the outer shell around  $M(r) \sim 35M_{\odot}$  can be observed by the emergence of  $^{28}\text{Si}$  near the former shock breakout region during pulsation. The outer shell at  $M(r) > 35 M_{\odot}$  is mostly  $^4\text{He}$  with a trace amount of  $^{12}\text{C}$ .

The  $Y_e$  profile shows  $Y_e \sim 0.46$  in the Fe core and sharp transition to  $Y_e = 0.5$  at  $M(r) > 5 M_{\odot}$ .

The density profile reveals a three-layer structure of the pre-supernova: the Fe-core at  $M(r) < 2 M_{\odot}$ , the Si-O envelope at  $M(r) = 2 - 35 M_{\odot}$ , and the outer He-shell at  $M(r) > 35 M_{\odot}$ . On the other hand, the temperature profile shows only the core and the envelope structure with no sharp gradient around the He-O interface. The Fe-core features a sharp drop of density of 5 orders of magnitude. The Si-O envelope has a shallow density gradient from  $10^5$  to  $10^3 \text{ g cm}^{-3}$ . The transition to the outer He-shell is shown by the sharp density change. The density also drops sharply towards the surface.

The velocity profile in the Fe core shows homologous contraction at  $M(r) < 2M_{\odot}$  with a peak velocity at  $1.8 \times 10^8 \text{ cm s}^{-1}$ . Then the velocity is zero at  $M(r) \sim 5M_{\odot}$ . At  $M(r) > 5 M_{\odot}$  the star is close to hydrostatic.

### 2.2. Methods of Nucleosynthesis and Radiative Transfer

For the progenitor model as described in 2, we first perform the hydrodynamical calculations of nucleosynthesis using the one-dimensional code described in Tominaga et al. (2007). The shock wave is calculated

<sup>2</sup> In the default setting of MESA (Paxton et al. 2017), the isotope  $^{56}\text{Cr}$  ( $Y_e = 0.43$ ) is used as a representative of electron capture products when the stellar core reaches a temperature sufficient for nuclear statistical equilibrium. This can keep the stellar evolutionary model achievable in a reasonable computational time. We remind that in general a wide range of isotopes with different neutron-proton ratios is necessary to capture the self-consistent electron capture rate. However, a large reaction network can make the general hydrodynamical treatment numerically demanding.

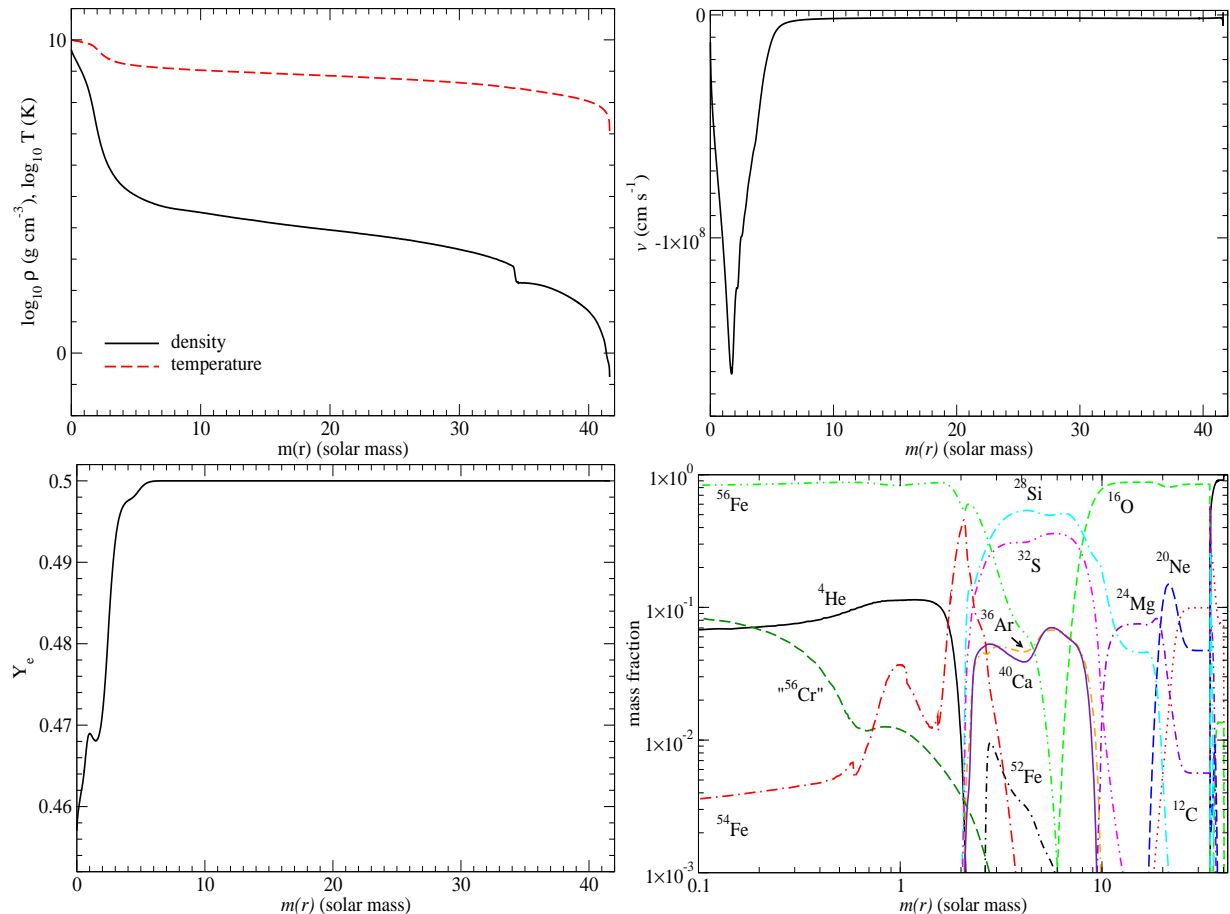


**Figure 2.** The density and temperature (top left), velocity (top right), electron mole fraction (bottom left) and abundance (bottom right) of the supernova model at the onset of collapse.

with the PPM method. Nucleosynthesis is calculated with the  $\alpha$ -network (13 species) coupled with the hydrodynamics and with a big network (280 species) for a post-processing.

For the bolometric light curve calculation, we use the radiation hydrodynamics code (SNEC) (Morozova et al. 2015). The code calculates the transport of blackbody radiation in the diffusion limit to obtain the bolometric light curve. The opacity takes the Rosseland mean opacity mainly from the OPAL tables (Iglesias & Rogers 1993, 1996). The ionization is obtained by solving the Saha equation. For the equation of state (EOS), the Paczynski EOS (Paczynski 1983) is adopted. The gamma-ray heating from the decays of radioactive  $^{56}\text{Ni}$  and  $^{56}\text{Co}$  is calculated assuming the gray transfer approximation and pure absorptive opacity.

### 3. EXPLOSIVE NUCLEOSYNTHESIS AND RADIOACTIVE HEATING

#### 3.1. Explosive Nucleosynthesis

For the optimized model in this paper, we set a thermal bomb at the mass cut at  $M_{\text{cut}} = 2.0 M_{\odot}$  with the

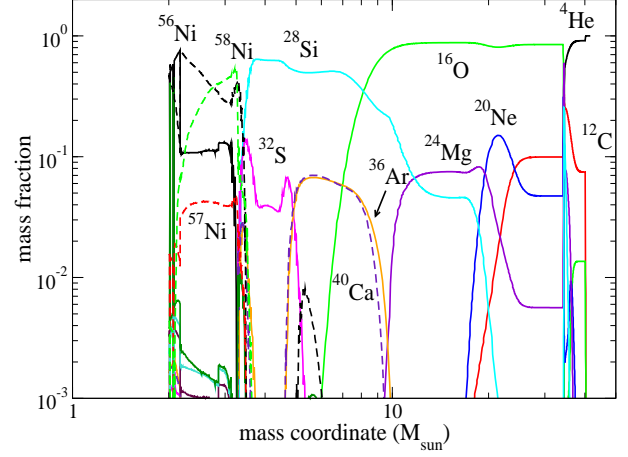
internal energy to make a kinetic energy of explosion (hereafter "explosion energy")  $E = 5 \times 10^{51} \text{ erg s}^{-1}$ . We then calculate the propagation of a shock wave coupled with nucleosynthesis. Nuclear energy release is added to  $E$  but negligibly small.

Figure 3 shows the distributions of the post-shock temperature and density at  $t = 50 \text{ s}$ , where  $t$  denotes the time after the thermal bomb is deposited.  $Y_e$  does not change from the presupernova values because of the low density in the ejecta.

The core from  $M_{\text{cut}}$  to  $\sim 3 M_{\odot}$  contains iron-peak nuclei including mostly  $^{56-58}\text{Ni}$  and  $^4\text{He}$  synthesized in the  $\alpha$ -rich freezeout. The middle layer at  $M(r) = \sim 3 - 10 M_{\odot}$  is occupied by intermediate mass species including  $^{28}\text{Si}$ ,  $^{32}\text{S}$ ,  $^{36}\text{Ar}$  and  $^{40}\text{Ca}$ . The inner envelope at  $M(r) \sim 10 - 35 M_{\odot}$  contains mostly light elements mostly  $^{16}\text{O}$ , and then  $^{20}\text{Ne}$  and  $^{24}\text{Mg}$ . At the surface there are unburned  $^4\text{He}$  and a small fraction of  $^{12}\text{C}$ . In Table 3.1, we summarize nucleosynthesis yields of radioactive nuclei at  $t = 50 \text{ s}$  and several species after radioactive decays. In particular, the amount of  $^{56}\text{Ni}$  is  $0.62 M_{\odot}$ .

**Table 1.** The ejecta mass and scaled abundance fraction of the star after explosive nucleosynthesis where all exothermic nuclear reaction has stopped. All masses are in units of  $M_{\odot}$ .

Isotope	A	Z	$(X_i/^{56}\text{Fe})/(X_i/^{56}\text{Fe})_{\odot}$	Mass
$^{12}\text{C}$	12	6	1.06	1.91
$^{13}\text{C}$	13	6	$2.11 \times 10^{-13}$	$4.55 \times 10^{-15}$
$^{14}\text{N}$	14	7	$1.10 \times 10^{-8}$	$4.77 \times 10^{-9}$
$^{15}\text{N}$	15	7	$5.07 \times 10^{-10}$	$8.72 \times 10^{-13}$
$^{16}\text{O}$	16	8	5.56	22.07
$^{17}\text{O}$	17	8	$7.76 \times 10^{-11}$	$1.23 \times 10^{-13}$
$^{18}\text{O}$	18	8	$1.12 \times 10^{-8}$	$1.02 \times 10^{-10}$
$^{19}\text{F}$	19	9	$2.11 \times 10^{-9}$	$4.21 \times 10^{-13}$
$^{20}\text{Ne}$	20	10	1.88	1.174
$^{21}\text{Ne}$	21	10	$1.09 \times 10^{-9}$	$2.17 \times 10^{-12}$
$^{22}\text{Ne}$	22	10	$1.24 \times 10^{-10}$	$1.04 \times 10^{-11}$
$^{23}\text{Na}$	23	11	$1.81 \times 10^{-7}$	$3.36 \times 10^{-9}$
$^{24}\text{Mg}$	24	12	3.84	1.04
$^{25}\text{Mg}$	25	12	$7.93 \times 10^{-7}$	$2.86 \times 10^{-8}$
$^{26}\text{Mg}$	26	12	$2.34 \times 10^{-5}$	$9.68 \times 10^{-7}$
$^{27}\text{Al}$	27	13	$3.43 \times 10^{-4}$	$1.06 \times 10^{-5}$
$^{28}\text{Si}$	28	14	10.12	3.52
$^{29}\text{Si}$	29	14	0.517	$9.51 \times 10^{-3}$
$^{30}\text{Si}$	30	14	$1.11 \times 10^2$	1.39
$^{31}\text{P}$	31	15	$2.96 \times 10^{-4}$	$8.05 \times 10^{-7}$
$^{32}\text{S}$	32	16	0.515	0.106
$^{33}\text{S}$	33	16	2.81	$4.75 \times 10^{-3}$
$^{34}\text{S}$	34	16	18.00	0.174
$^{36}\text{S}$	36	16	0.696	$2.30 \times 10^{-5}$
$^{35}\text{Cl}$	35	17	0.218	$3.68 \times 10^{-4}$
$^{37}\text{Cl}$	37	17	0.489	$2.83 \times 10^{-4}$
$^{36}\text{Ar}$	36	18	5.17	0.224
$^{38}\text{Ar}$	38	18	4.73	$4.05 \times 10^{-2}$
$^{40}\text{Ar}$	40	18	$2.30 \times 10^{-2}$	$2.48 \times 10^{-6}$
$^{39}\text{K}$	39	19	0.151	$2.60 \times 10^{-4}$
$^{40}\text{K}$	40	19	0.213	$5.54 \times 10^{-7}$
$^{41}\text{K}$	41	19	1.50	$2.00 \times 10^{-4}$
$^{40}\text{Ca}$	40	20	6.55	0.214
$^{42}\text{Ca}$	42	20	1.06	$2.40 \times 10^{-4}$
$^{43}\text{Ca}$	43	20	0.257	$1.36 \times 10^{-5}$
$^{44}\text{Ca}$	44	20	2.53	$1.94 \times 10^{-3}$
$^{46}\text{Ca}$	46	20	$2.91 \times 10^{-3}$	$3.72 \times 10^{-9}$
$^{48}\text{Ca}$	48	20	$9.04 \times 10^{-10}$	$6.80 \times 10^{-14}$
$^{45}\text{Sc}$	45	21	$8.94 \times 10^{-2}$	$1.68 \times 10^{-6}$
$^{46}\text{Ti}$	46	22	0.462	$5.45 \times 10^{-5}$
$^{47}\text{Ti}$	47	22	0.554	$6.15 \times 10^{-5}$
$^{48}\text{Ti}$	48	22	1.99	$2.29 \times 10^{-3}$
$^{49}\text{Ti}$	49	22	0.418	$3.65 \times 10^{-5}$
$^{50}\text{Ti}$	50	22	0.223	$1.93 \times 10^{-5}$
$^{50}\text{V}$	50	23	7.60	$3.13 \times 10^{-6}$
$^{51}\text{V}$	51	23	3.86	$6.71 \times 10^{-4}$



**Figure 3.** The distributions of the chemical abundances at  $t = 50$  s after the thermal bomb is deposited at  $M_{\text{cut}} = 2.0M_{\odot}$  to produce  $E = 5 \times 10^{51}$  erg  $\text{s}^{-1}$ .

**Table 2.** (*cont'd*) The ejecta mass and scaled abundance fraction of the star after explosive nucleosynthesis where all exothermic nuclear reaction has stopped. All masses are in units of  $M_{\odot}$ . A and Z are the atomic mass and number of the isotopes.

Isotope	A	Z	$(X_i/^{56}\text{Fe})/(X_i/^{56}\text{Fe})_{\odot}$	Mass
$^{50}\text{Cr}$	50	24	9.26	$3.41 \times 10^{-3}$
$^{52}\text{Cr}$	52	24	7.38	$5.49 \times 10^{-2}$
$^{53}\text{Cr}$	53	24	2.50	$2.16 \times 10^{-3}$
$^{54}\text{Cr}$	54	24	0.492	$1.08 \times 10^{-4}$
$^{55}\text{Mn}$	55	25	1.56	$1.07 \times 10^{-2}$
$^{54}\text{Fe}$	54	26	4.73	0.181
$^{56}\text{Fe}$	56	26	1.00	0.623
$^{57}\text{Fe}$	57	26	3.26	$4.94 \times 10^{-2}$
$^{58}\text{Fe}$	58	26	$9.29 \times 10^{-3}$	$2.16 \times 10^{-5}$
$^{59}\text{Co}$	59	27	1.41	$2.47 \times 10^{-3}$
$^{58}\text{Ni}$	58	28	14.74	0.374
$^{60}\text{Ni}$	60	28	2.01	$2.04 \times 10^{-2}$
$^{61}\text{Ni}$	61	28	4.70	$2.20 \times 10^{-3}$
$^{62}\text{Ni}$	62	28	41.51	$6.07 \times 10^{-2}$
$^{64}\text{Ni}$	64	28	$1.41 \times 10^{-8}$	$6.29 \times 10^{-12}$
$^{63}\text{Cu}$	63	29	0.474	$1.50 \times 10^{-4}$
$^{65}\text{Cu}$	65	29	$2.28 \times 10^{-4}$	$3.34 \times 10^{-8}$
$^{64}\text{Zn}$	64	30	$1.66 \times 10^{-2}$	$8.77 \times 10^{-6}$
$^{66}\text{Zn}$	66	30	$1.86 \times 10^{-6}$	$5.60 \times 10^{-10}$
$^{67}\text{Zn}$	67	30	$7.11 \times 10^{-8}$	$3.29 \times 10^{-12}$
$^{68}\text{Zn}$	68	30	$1.11 \times 10^{-8}$	$2.38 \times 10^{-12}$
$^{70}\text{Zn}$	70	30	$1.48 \times 10^{-7}$	$1.09 \times 10^{-12}$



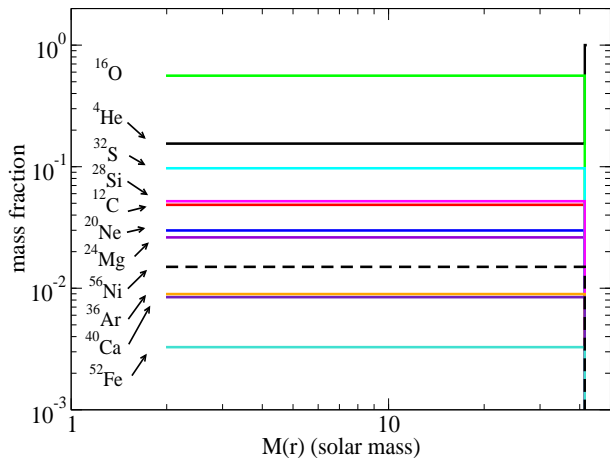


**Figure 4.** The abundance pattern of the ejecta and CSM adopted in the optimized model (See next plot). The ejecta is assumed to be completely mixed as a representation of aspherical explosion.

### 3.2. Radioactive Decays and Light Curve

In the adopted PPISN model, the power sources of the optical light curve are circumstellar interaction (Section 4) and radioactive decays of  $^{56}\text{Ni}$  and  $^{56}\text{Co}$ . In Figure 5, several theoretical LCs are compared with the observed light curve of AT2018cow (Perley et al. 2019). For the radioactive decay light curve models in Figure 5, we adopt  $\kappa_\gamma = 0.06 Y_e \text{ cm}^2 \text{ g}^{-1}$ .

(1) The dash-dotted purple curve is the bolometric light curve powered by circumstellar interaction only (see section 4) without radioactive decays. The opacity are calculated for the original abundance distribution (Fig. 3). This light curve can reproduce the observed light curve for only the first 20 days.

(2) The dotted-red curve shows the bolometric light curve powered by radioactive decays without circumstellar interaction for the original (centered) distribution of  $0.62 M_\odot$   $^{56}\text{Ni}$  (Fig. 3). Its peak luminosity reaches only  $\sim 10^{41.5} \text{ erg s}^{-1}$ , which is too faint to explain the observations. This implies it takes too long time for radioactive heat to reach the surface because of massive ejecta.

(3) The above comparison suggests that extensive mixing of  $^{56}\text{Ni}$  to the surface takes place possibly by a jet-like explosion. We thus make a simple assumption that the ejecta is uniformly mixed from the mass cut of  $M(r) = 2 M_\odot$  to the surface of  $M(r) = 41.60 M_\odot$ . The uniform abundance distribution is shown in Figure 4. The calculated bolometric light curve is shown by the dashed-green curve. Thanks to the  $^{56}\text{Ni}$  heating in the outer layers, the light curve is consistent with the observations at  $t > 25$  days.

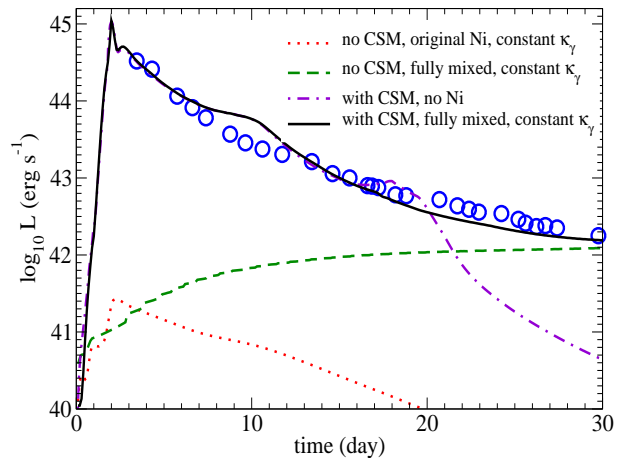


**Figure 5.** Bolometric light curves powered by the radioactive decays of  $^{56}\text{Ni}$  and  $^{56}\text{Co}$  for various abundance distributions are shown to compare with the data points (blue circles) observed from AT2018cow (Perley et al. 2019). The red dotted line and green dashed line show the light curve models for the original  $^{56}\text{Ni}$  distribution and the uniformly mixed one, respectively. Here no circumstellar interaction is included. For gamma-ray transport,  $\kappa_\gamma = 0.06 Y_e \text{ g cm}^{-2}$  is adopted. For comparison, the black solid line shows the light curve powered by circumstellar interaction but no  $^{56}\text{Ni}$  in the ejecta. The purple dot-dash line shows a similar light curve but assumes all isotopes in the ejecta is fully mixed, including  $^{56}\text{Ni}$ .

(4) The solid-black curve shows the bolometric light curve with the combined powers of circumstellar interaction and radioactive decays. The uniform abundance distribution is adopted (Figure 4) to calculate the radioactive heating and opacity. The calculated light curve is in good agreement with the observed light curve of AT2018cow. The later light curve at  $t > 20$  days declines slower than AT2018cow, which will be discussed in section. We thus adopt the uniform abundance distribution in Figure 4 for the model which we call the “optimized” model.

## 4. CIRCUMSTELLAR INTERACTION

### 4.1. Formation and Structure of Circumstellar Matter

In calculating the light curve powered by circumstellar interaction, we adopt the He star model of  $M_{\text{He}} = 42.10 M_\odot$ , which undergoes PPI and ejects He-rich surface materials to form CSM of mass  $M_{\text{CSM}} = 0.50 M_\odot$  at  $\sim 1.6$  year prior to its collapse (see Introduction). Thus the He star has  $M_{\text{He}} = 41.60 M_\odot$  at the beginning of Fe core collapse.

We plot in Figure 5 the bolometric light curve using the chemical distribution shown in Figure 4. We also present contrasting models to demonstrate the individual contributions of CSM and  $^{56}\text{Ni}$ -decay. We assume

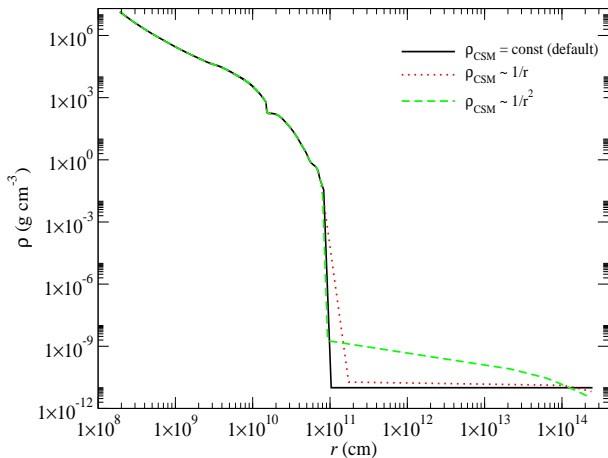


**Figure 6.** The stellar and CSM density profiles of the initial models. The black-solid line shows the optimized model. Other lines show those for comparisons in section 5. All models have the same CSM mass  $M_{\text{CSM}} = 0.50 M_{\odot}$  and an outer CSM radius  $R_{\text{CSM}} \sim 10^{14}$  cm.

that CSM has a constant density of  $\rho_{\text{CSM}} = 10^{-11}$  g cm $^{-3}$  extending to  $R_{\text{CSM}} \sim 10^{14}$  cm as seen in Figure 6. Note such CSM is optically thick. We examine in section 5 how the shape of the bolometric light curve depends on  $M_{\text{CSM}}$ ,  $\rho_{\text{CSM}}$ , and  $R_{\text{CSM}}$ , and how the comparison with AT2018cow provides constraints on these quantities.

Spectroscopic observations of AT2018cow have reported the appearance of H-features in the spectra  $\sim 15$  days after the light maximum (Perley et al. 2019). The existence of some H in the ejecta and CSM can be explained as follows. During the evolution, the progenitor star of the PPISN loses a large fraction of its massive H envelope (e.g., Leung et al. 2019). The exact amount of H which remains in the progenitor depends strongly on the mass, metallicity, and binarity of the progenitor. If some amount of H remains in the star when the mass ejection due to PPI occurs, CSM of the PPISN contains some H.

Another possibility that some H exist in CSM is the case where H-rich environment has been formed outside the progenitor star. During the ejection of the He envelope due to PPI, the high velocity He-shell may interact with the surrounding low velocity H-rich materials. The deceleration of the He shell causes Rayleigh-Taylor instabilities and some H-rich matter is mixed into the He shell.

We also examine in section 5 how the existence of H affects the light curve shape

#### 4.2. Hydrodynamical Evolution of Shock Propagation

We start the radiation hydrodynamical simulation from the Fe core collapse. A shock wave is generated by

inserting a thermal bomb at the mass cut  $M_{\text{cut}} = 2 M_{\odot}$  with the explosion energy  $E = 5 \times 10^{51}$  erg. The elemental abundance profile obtained from the explosive nucleosynthesis calculation (Figure 3) is assumed to be uniformly mixed (Figure 4).

In Figure 7 we plot the distributions of the density (top left panel), velocity (top right panel), temperature (middle left), free electron fraction (middle right), optical depth (bottom left) and luminosity profile (bottom right) for the optimized model at Day 0 (solid black line), 1 (red dotted line), 5 (green dashed line), 10 (blue long-dashed line), 20 (purple dot-dash line) and 30 (cyan dot-long dash line) after the formation of the shock wave. Here CSM at  $M(r) = 41.6 - 42.1 M_{\odot}$  is included.

*Density ( $\rho$ ):* The initial density profile is the pre-collapse profile shown in Figure 2 and the  $0.50 M_{\odot}$  CSM with a constant density of  $10^{-11}$  g cm $^{-3}$  extending to  $\sim 10^{14}$  cm as seen in Figure 6. We note that CSM is optically thick. At Day 1, the shock wave has arrived at the inner radius of CSM and enhanced the density there by two orders of magnitude. At Day 2, the shock-breakout from CSM occurs. At Day 5, the post-shock structure develops with a trough inside the inner CSM and a bump just behind CSM. A reverse shock can be seen around Day 10, but it freezes when the free expansion of matter dominates the motion.

*Velocity ( $v$ ):* When the shock wave arrives at CSM at Day 1, the velocity at the inner edge of CSM reaches as high as  $1.4 \times 10^9$  cm s $^{-1}$ , while the outer part of CSM is close to static. During the propagation, the shock wave transfers its momentum to the CSM as seen in the profile at Day 3. Because of the much smaller mass, CSM gets a velocity of  $1.5 \times 10^9$  cm s $^{-1}$  which is much higher than  $8 \times 10^8$  cm s $^{-1}$  in the He star. Most of the star has already developed homologous expansion after Day 5, except a small non-vanishing reverse shock near the inner boundary of CSM.

*Temperature ( $T$ ):* The compact pre-collapse He star has a surface temperature as high as  $\sim 10^7$  K. The CSM is assumed to be isothermal at  $10^4$  K. When the shock wave reaches the inner boundary of the CSM at Day 1, the surface temperature has already cooled down to  $< 10^5$  K, while the shock heated matter can be as hot as  $2 \times 10^5$  K. At Day 5, the hot temperature bump smears out due to diffusion. Around Day 20, both the star and CSM become isothermal.

*Free electron fraction ( $X_e$ ):*  $X_e$  is an important factor for the opacity since a free electron has a small but constant cross-section, compared to other bound-free and bound-bound transitions, which strongly depend on the population of particular ionization stages. At the begin-

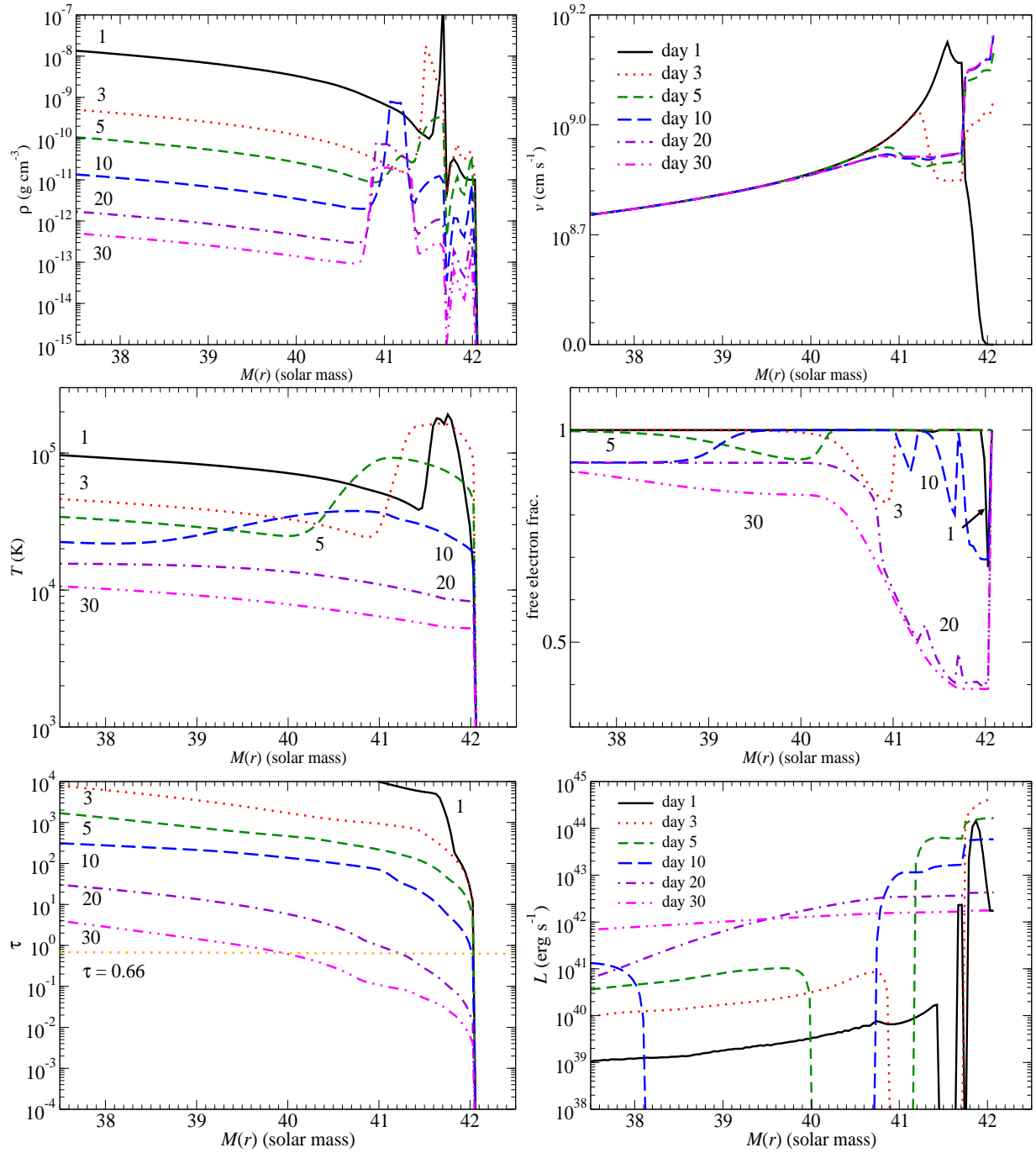


**Figure 7.** The density (top left), velocity (top left), temperature (middle left), free electron fraction (middle right), optical depth (bottom left) and luminosity (bottom right) of the benchmark model at Day 1 (solid black line), 1 (red dotted line), 5 (green dashed line), 10 (blue long-dashed line), 20 (purple dot-dash line) and 30 (magenta dot-dot-dash line) after the injection of energy.



ning, the star is completely ionized, while the CSM is less ionized with a fraction of  $\sim 40\%$ . Once the shock wave reaches the surface the heat allows the rapid ionization of the CSM. At Day 5, when the reverse shock is propagating backward, the matter near the outer layer of the star has a low enough density and temperature for recombination. At Day 10, the recombination region is more extended. The shocked heated front remains fully ionized but the whole profile is bumpy, because of the shock-induced density fluctuations. At Day 20, when the photosphere starts to recede, CSM cools down and more matter has recombined. At Day 30, the whole ejecta gradually recombines.

*Optical depth ( $\tau$ ):* Initially, the star and CSM are opaque, having  $\tau > 1$  except at the very shallow layer just below the stellar surface. As the star expands,  $\tau$  decreases. However, the shock front makes the opacity sufficiently high that the photosphere remains at the outermost part of the star. By Day 20, the photosphere gradually retreats to  $M(r) \sim 40 M_{\odot}$ . At Day 30 the photosphere receded much deeper into the star, showing that the ejecta gradually becomes transparent.

*Luminosity ( $L(r)$ ):* When the shock starts to interact with CSM, the luminosity profile becomes extremely bumpy because of the fluctuations of the temperature, density, free electron fraction, and thus opacity because of shock propagation. At Days 3 and 5 the stellar surface becomes the most brightest part of the star. However, the trough in luminosity develops when the reverse shock allows an early recombination of atoms. Beyond Day 20, the luminosity profile has reached a steady state that radiation develops steadily and reaches a uniform luminosity at Day 30. The photosphere recedes by  $\sim 1 M_{\odot}$  per 10 days.

#### 4.3. Radiation Hydrodynamical Results

In Figure 8 we plot the radiation hydrodynamical results of our “optimized” model, i.e., the bolometric luminosity (top left panel), effective temperature (top right panel), photospheric radius (bottom left panel) and velocity at the photosphere (bottom right panel). The solid lines show the model with the circumstellar interaction as described in the earlier subsection. When the shock-breakout from the optically thick CSM occurs at Day 2, the bolometric luminosity reaches the bright peak. Then the luminosity rapidly declines through radiative cooling. Such a sharp rise to a bright peak and a rapid decline of the light curve well reproduce the observed FBOT-like feature of AT2018cow (Perley et al. 2019). After day 18, the luminosity would decrease too rapidly, if there would be no radioactive heating as already shown in Figure 5.

For comparison, the results for the model without CSM are shown by the dashed curve. There is no sign of shock-breakout where the light curve is smooth and flat. Its luminosity around Day 2 is almost 3 orders of magnitude lower than the peak due to circumstellar interaction, but it reaches an asymptotic value of  $\sim 10^{42}$  erg s $^{-1}$  at Day 20.

Then the bolometric light curve produced by the combined powers of circumstellar interaction and the radioactive decays shows a good agreement with AT2018cow. The effect of shock heated CSM is seen in the luminosity evolution.

However, the observed temperature and radius at the photosphere of AT2018cow monotonically decrease (Perley et al. 2019), which suggests that the photosphere recedes inward in  $M(r)$  at a pace different from the model. Such a difference in the local quantities at the photosphere might stem from a possible aspherical structure of CSM and the ejecta of AT2018cow. It would be interesting to investigate the radiation hydrodynamics of a multi-D structure of CSM-ejecta.

#### 4.4. Spectral Evolution of AT2018cow

Although we focus on mainly reproducing the evolution of the bolometric flux from AT2018cow, our optimized model broadly outlines also some aspects of its spectral evolution (Prentice et al. 2018; Perley et al. 2019).

According to the observations, the spectra of AT2018cow are very blue and almost featureless in the beginning, for days 4 to 8 after the maximum (Perley et al. 2019), which roughly corresponds to Days 7 to 11 after the explosion. This is exactly what we expect to see in our optimized model. The optical depth in Figure 8 shows that on Day 10 the photosphere is located in the outermost layers of CSM. These layers are shock-heated to about 20,000 K at this time. The continuum emission must be very bright under such conditions, and optical lines, even if some of them were formed at so high temperature, sink under the continuum level.

Between Days 10 and 20, the photosphere starts to dive back into the ejecta layers, while the temperature falls down to 9,000–10,000 K. The conditions become more suitable for forming optical lines, and exactly during this period they appear in the spectrum of AT2018cow.

The problem arises with the explanation of weak narrow components of lines that are often observed after Day 20 in the spectra of AT2018cow. These lines do not appear in the ejecta and CSM of the optimized model, because all materials in the model are already accelerated to velocities as high as 7,000 - 13,000 km s $^{-1}$ .

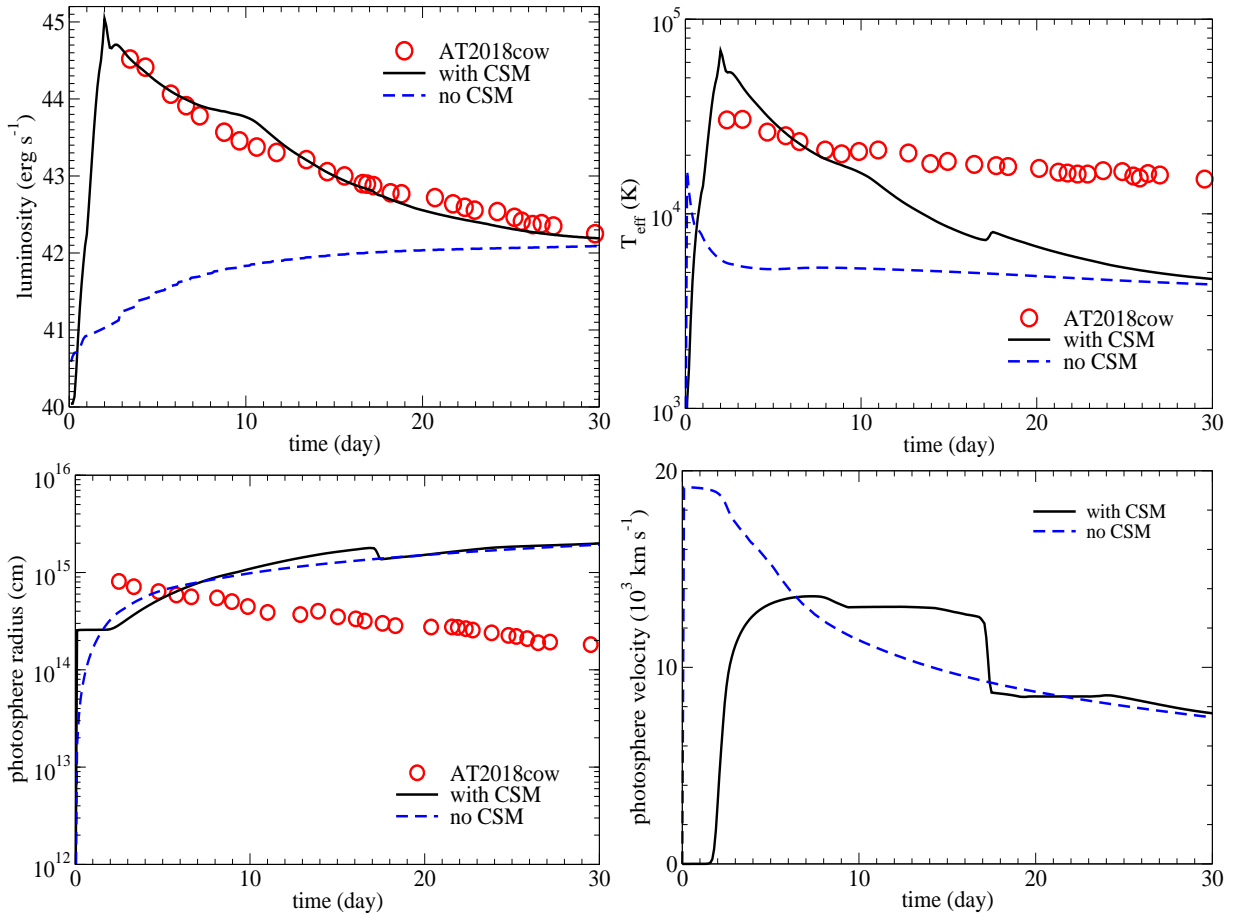


**Figure 8.** The luminosity (top left), effective temperature (top right), photosphere radius (bottom left), velocity at the photosphere (bottom right) against time for the optimized model. The models with and without CSM predicted by the stellar evolutionary models are shown. The data points correspond to those from AT2018cow (Perley et al. 2019).

But these weak components do not resemble the typical shape of the lines of Type II<sub>n</sub> supernovae (SNe II<sub>n</sub>). These are much weaker than in SNe II<sub>n</sub>. We suppose that these weak lines must not arise from the spherical envelope, into which the exploding object is embedded, as it happens in SN II<sub>n</sub>'s. Instead, these lines can be emitted, for example, by more extended nearby (possibly a disk-shaped) structure lost by the progenitor much earlier, having low velocity and illuminated by the explosion.

The late appearance of hydrogen lines (Perley et al. 2019) is expected by such extended CSM with hydrogen that was lost earlier (subsection 4.1). As will be shown in Section 5.5 and Figure 6, when we admix large amount of hydrogen into the helium CSM, this affects the bolometric light curve very weakly.

## 5. DEPENDENCE OF LIGHT CURVE ON MODEL PARAMETERS

### 5.1. The Comparison Model

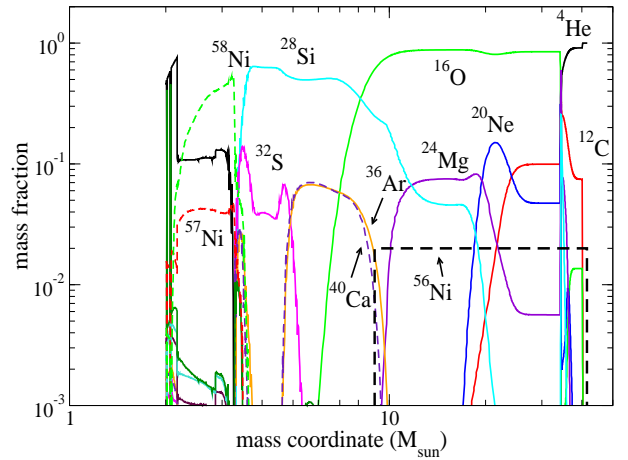


**Figure 9.** The abundance distribution adopted in the “comparison” model used for the parameter study in this section. It assumes that only radioactive  $^{56}\text{Ni}$  is brought to the outer layers of  $M(r) = 9.0 - 41.6M_{\odot}$ .

In the previous section we have studied how the combined powers of circumstellar interaction and radioac-

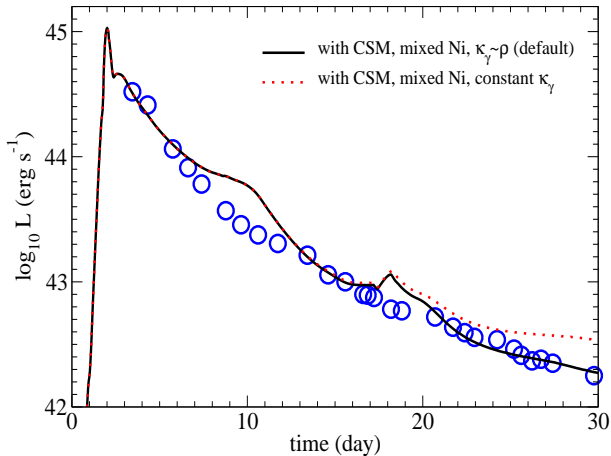


**Figure 10.** The black-solid line shows the bolometric light curve of the “comparison” model based on the abundance distribution in Figure 9 (see text) as compared with the observed data of AT2018cow (Perley et al. 2019). For radioactive heating, the black-solid line adopts  $\kappa_\gamma = 0.06Y_e$   $\text{g cm}^{-2}(\rho/\rho_0) \text{ cm}^2 \text{ g}^{-1}$  if  $\rho < \rho_0 = 10^{-10} \text{ g cm}^{-3}$ . If the constant  $\gamma$ -ray opacity  $\kappa_\gamma = 0.06Y_e \text{ g cm}^{-2}$  is adopted, the light curve is shown by the red-dotted line, whose decline is too slow to be compatible with AT2018cow.

tive decays can explain the bolometric light curves of AT2018cow and obtained the “optimized” model.

We should note that the theoretical bolometric light curve depends on a number of parameters and assumptions adopted in the modeling. Here, we study how the light curves depend on the choice of these parameters.

For these comparison studies, we construct a “comparison” model whose bolometric light curve is in fairly good agreement with AT2018cow but with a different set of model parameters from the “optimized” model. In this “comparison” model, the elemental abundance distribution in Figure 9 is assumed. Here the original abundance distribution is adopted to calculate the equation of state and opacities except for radioactive  $^{56}\text{Ni}$  which is moved to the outer layers at  $M(r) = 9.0 - 41.6 M_\odot$ . The aim is to study the enhanced heating effects of  $^{56}\text{Ni}$  by mimicking the jet-like ejection of  $^{56}\text{Ni}$ -rich region from a deeper layer.

In Figure 10, the bolometric light curve for this “comparison” model is shown by the black-solid line compared with the observed data of AT2018cow (Perley et al. 2019). For radioactive heating, the “comparison” model (black-solid line) adopts a  $\kappa_\gamma = 0.06Y_e$   $\text{g cm}^{-2}(\rho/\rho_0) \text{ cm}^2 \text{ g}^{-1}$  if  $\rho < \rho_0 = 10^{-10} \text{ g cm}^{-3}$ . If the constant  $\gamma$ -ray opacity  $\kappa_\gamma = 0.06Y_e \text{ g cm}^{-2}$  is adopted, the light curve is shown by the red-dotted line, whose decline is too slow to be compatible with AT2018cow. The reduction of  $\kappa_\gamma$  at low densities could mimic the effects of clumpy density distribution (e.g., Eq.(1) of

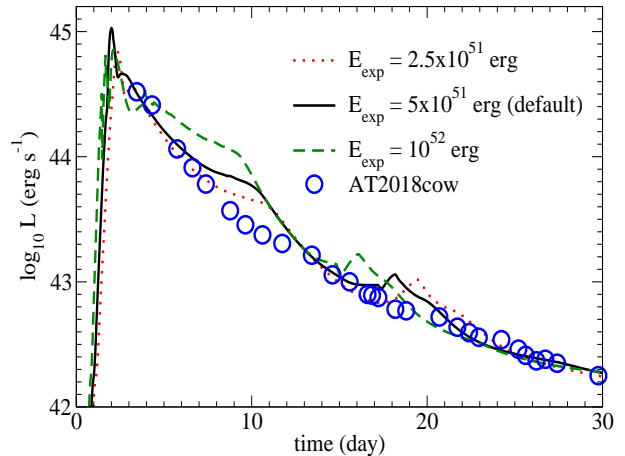


**Figure 11.** Light curves of the comparison model with  $E = 5 \times 10^{51}$  erg and its variations with different explosion energy. The data points correspond to those from AT2018cow.

Kumagai et al. 1989) in the ejecta. Because the black-solid curve is in better agreement with the late-time data of AT2018cow, we treat this “comparison” model as a default model for comparison.

### 5.2. Dependence on Explosion energy

In the light curve calculation, we treat the kinetic energy of explosion  $E$  as a model parameter. Theoretically, the explosion mechanisms of the core-collapse supernovae are not well-understand. Thus it is not certain how much explosion energy is given to the ejecta. For example, if a black hole is formed with an accretion disk around it, a powerful bipolar jet from magnetohydrodynamical instabilities may provide a large amount of energy to the ejecta. Without actual modeling of a core-collapse supernova, it would be useful to constrain the explosion energy from the light curve modeling. Here we examine how the light curve depends on the explosion energy. We thus search the explosion energy from  $E = 10^{51}$  to  $10^{52}$  erg which produces the closest light curve to AT2018cow.

In Figure 11 we plot the light curves for the comparison model with an explosion energy of  $E = 2.5 \times 10^{51}$ ,  $5 \times 10^{51}$  and  $10^{52}$  erg, respectively. Other parameters, such as the CSM profile and the resolution are the same as the comparison model. It is seen that the effects of explosion energy is secondary. It does not play an important role in the shock-breakout time and the peak luminosity. It affects a little the post-maximum decrease and the fluctuations of the luminosity. The model with a higher explosion energy fades slower, because the stronger shock makes the post-shock density higher, thus making the recession of the photosphere slower.

### 5.3. Dependence on CSM Structure

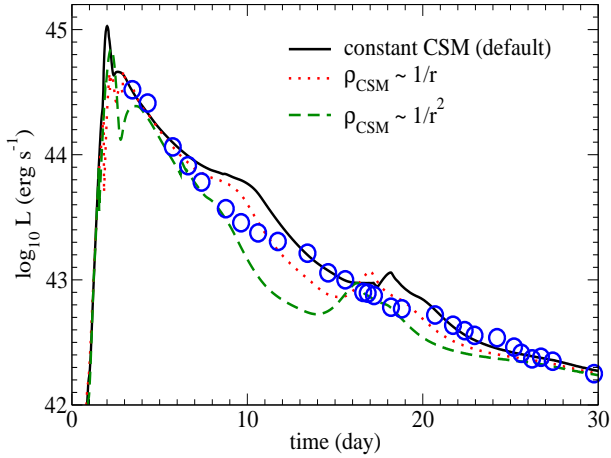


**Figure 12.** Light curves of the default model and its variations with different CSM density profiles. The blue circles show the observed data of AT2018cow.

The comparison model is assumed to have CSM with a constant density of  $10^{-11} \text{ g cm}^{-3}$ . Here we examine how the light curve depends on the CSM density structure by adopting a profile of  $(1/r^\alpha)$  with  $\alpha = 0, 1$  and  $2$  as shown in Figure 6. In constructing the density profile, we require that CSM has the same mass  $\sim 0.5 M_\odot$  and the same outer radius as the comparison model.

In Figure 12 we plot the light curves for the comparison model (black-solid) and its variations with different CSM density profiles: i.e.,  $1/r$  (red dashed line) and  $1/r^2$  (green dot-dashed structure). It is seen that qualitatively the light curve is not sensitive to the CSM density profile. The steeper CSM density results in a quicker decrease in the luminosity and a lower luminosity peak. The late luminosity evolution becomes very close to each other and overlaps when the  $^{56}\text{Co}$  decay dominates the light curve.

#### 5.4. Dependence on CSM Density

Here we examine the dependence on the CSM density  $\rho_{\text{CSM}}$ .

We take the total mass of CSM is the same as comparison model and vary the inner and outer boundaries of CSM as two model parameters. In Figure 13 we plot the initial structure of the comparison model and those with the various CSM density from  $10^{-11}$  to  $10^{-9} \text{ g cm}^{-3}$ . For a higher  $\rho_{\text{CSM}}$ , the outer radius of CSM can be almost an order of magnitude smaller than the model with a lower  $\rho_{\text{CSM}}$ .

In Figure 14, we plot the corresponding light curves for the explosion models assuming the same explosion energy  $5 \times 10^{51} \text{ erg}$  and same resolution of mass grid  $0.04 M_\odot$  as the comparison model. The CSM density plays an important role in two aspects.

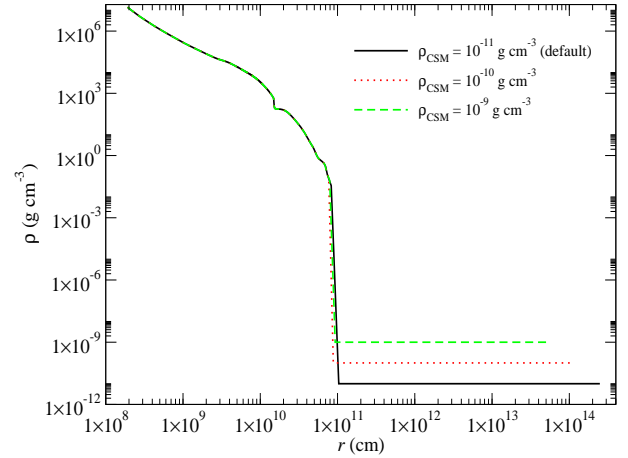


**Figure 13.** The initial stellar and CSM density profiles of the models comparing the effects of CSM density. All models have the same CSM mass  $0.5 M_\odot$  and a flat CSM profile.

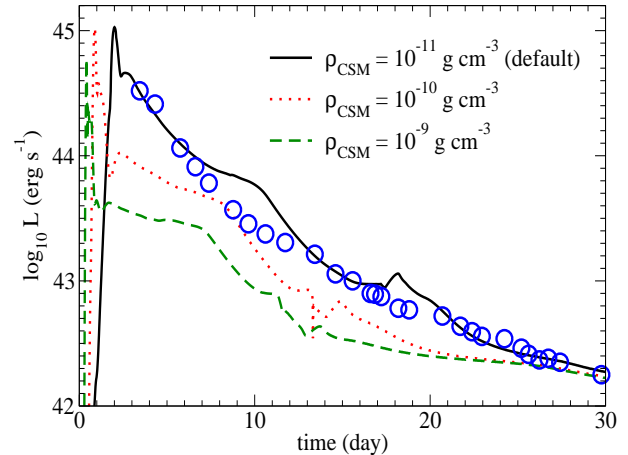


**Figure 14.** Light curves of the default model and its variations with different CSM density of  $10^{-10}$  (red dotted line) and  $10^{-11} \text{ g cm}^{-3}$  (green dashed line). The blue circles show the observed data of AT2018cow.

(1) First, the initial peak (shock breakout) depends sensitively on  $\rho_{\text{CSM}}$  and hence the outer radius of CSM. The first peak changes from Day 3 to Day 1 when  $\rho_{\text{CSM}}$  increases from  $10^{-11}$  to  $10^{-9} \text{ g cm}^{-3}$ , which corresponds to the decrease in the CSM outer radius from  $3 \times 10^{14} \text{ cm}$  to  $5 \times 10^{13} \text{ cm}$ .

(2) Second, the post-peak evolution before the  $^{56}\text{Co}$  decay is sensitive to  $\rho_{\text{CSM}}$ . For lower  $\rho_{\text{CSM}}$ , the post-peak fall in the luminosity is faster. It takes about 5 days for the comparison model ( $\rho_{\text{CSM}} = 10^{-11} \text{ g cm}^{-3}$ ) to decrease one order of magnitude in luminosity, compared to the one with higher  $\rho_{\text{CSM}} = 10^{-9} \text{ g cm}^{-3}$ , for which it takes about 10 days for the luminosity to decrease by one order of magnitude.

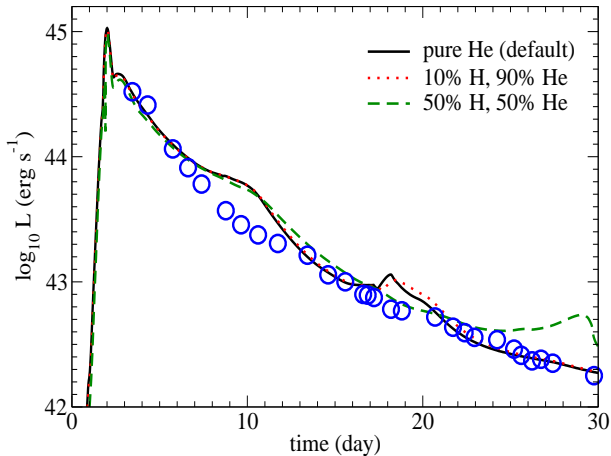


**Figure 15.** Light curves of the comparison model and the models that includes some hydrogen in CSM (10 % H and 50 % H). The blue circles show the observed data of AT2018cow.

### 5.5. Dependence on Hydrogen in CSM

In the spectra of AT2018cow, H-features appear  $\sim 15$  days after the light maximum (Perley et al. 2019). We then discuss in subsection 4.1 the formation scenario to have some H in the ejecta and CSM.

To examine the possible effects of H in CSM, we approximate the composition of CSM from pure He to two other abundances: a low H mixing (0.1 H and 0.9 He) and a high H mixing (H and He are 50 % by mass fraction).

In Figure 15 we plot the corresponding light curve with the data point from COW. The light curves are almost identical despite the photosphere still lies inside CSM. The model with the higher H mixing has a slightly lower bolometric luminosity at Day 18 despite a similar light curve shape. The effects of H only become observable in the H-rich model which shows a higher luminosity at Day 28 – 30.

### 5.6. Dependence on CSM Mass

The mass of CSM  $M_{\text{CSM}}$  depends on the dynamical mass loss during PPI, thus being sensitive to the progenitor mass. Here we examine how the light curve depends on  $M_{\text{CSM}}$  for the same  $R_{\text{CSM}}$  as of the comparison model.

In Figure 16 we plot the light curves for three models with  $M_{\text{CSM}}/M_{\odot} = 0.50$  (black solid line for the comparison model), 1.0 (red dotted line), and 2.0 (green dashed line), having the same  $R_{\text{CSM}}$ .

The light curve features depend strongly on  $M_{\text{CSM}}$ . Larger  $M_{\text{CSM}}$  delays the shock breakout of the light curve from Day 2 to about Day 3. The peak luminosity is also higher for larger  $M_{\text{CSM}}$ . The declining slope of the light curve becomes flatter when  $M_{\text{CSM}}$  is large. For

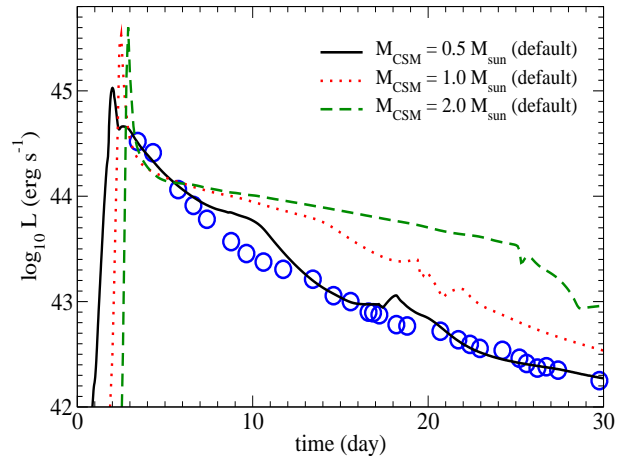


**Figure 16.** Bolometric light curves for  $M_{\text{CSM}}/M_{\odot} = 0.50$  (black solid; comparison), 1.0 (red dotted), and 2.0 (green dashed).  $R_{\text{CSM}}$  is fixed at  $\sim 2 \times 10^{14}$  cm. The blue circles show the observed data of AT2018cow.

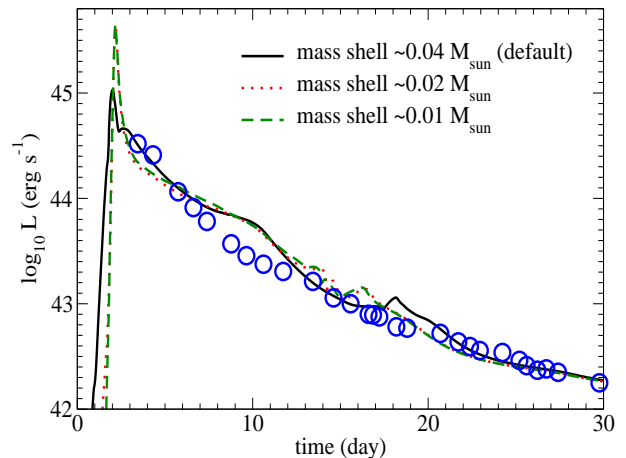


**Figure 17.** Light curves of the comparison model and its variations with different resolutions of the mass coordinate.

$M_{\text{CSM}} = 2.0M_{\odot}$ , the light curve remains  $\sim 10^{44}$  erg  $\text{s}^{-1}$  between day 5 – 25. As a result, the transition to the phase powered by  $^{56}\text{Co}$ -decay is also slightly delayed. These trends are the effects of a longer diffusion time in more massive CSM.

Our results confirm that  $M_{\text{CSM}}$  is strongly constrained by the light curve width, and as small as  $\sim 0.5M_{\odot}$  to be consistent with AT2018cow as Perley et al. (2019) has estimated.

### 5.7. Dependence on Resolution

How the shock propagates through the CSM controls the early evolution of the light curve. That means how the shock is resolved is important to trace how the kinetic energy of the shock is transformed to the internal energy and hence the blackbody radiation through shock



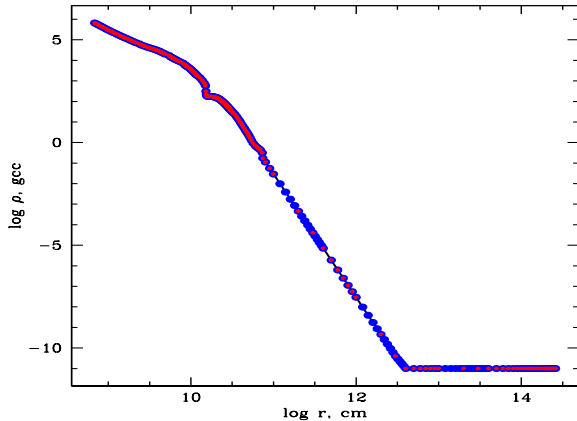


**Figure 18.** Initial density profile of the presupernova model for comparison (red stars) and its remapping for STELLA runs (blue dots).

compression. Here we examine how the results depend on the choice of the resolution.

In Figure 17 we plot the light curves of the comparison model with the current resolution (1000 grids), two times and four times higher resolutions. The highest resolution has a mass resolution of  $\sim 10^{-2} M_{\odot}$ . The qualitative features of the light curve are very well captured from the current resolution. The higher resolution has a higher maximum luminosity in the early peak, owing to the smaller mass shell. After the shock breakout, three models behave similarly, except when Day 20 the bump appears later when the resolution is lower. Despite that the similarity of the three light curves shows that the shock propagation is already well captured by the current resolution.

### 5.8. Comparison with STELLA

In this subsection we compare the numerical results with the multi-color radiative transfer calculation done by the code STELLA (Blinnikov et al. 2006; Baklanov et al. 2015). In the bulk of the present work we did not use STELLA because its implicit and multi-band nature makes the parameter searching for the optimized light curve unavoidably time-consuming.

Here we compare our results obtained from the black-body diffusion-limit radiative transport calculation by SNEC with the results computed by STELLA. We give comparisons only for the bolometric light curve of the comparison model described in subsection 5.1. The multi-band light curves calculated by STELLA for another set of models are presented in a separate publication (Sorokina et al., in preparation).

The presupernova model calculated by MESA has more than 1200 mesh zones. Blue dots in Figure 18 show

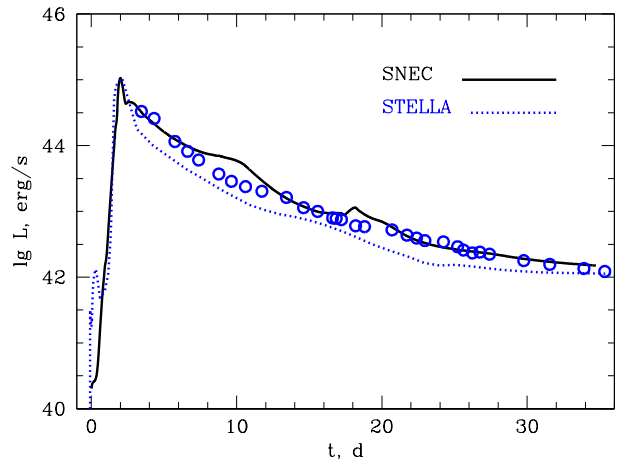


**Figure 19.** Bolometric light curves adopted by SNEC (thin line) and STELLA (dotted blue line) for the presupernova models shown in Figure 9.

our remapping of this model for STELLA runs with 232 zones, which is much more uniform than the one used for SNEC. It is clear that the resolution of the structure in interior is sufficiently high.

The both codes STELLA and SNEC are spherically symmetric Lagrangean radiation-hydrodynamic ones. Hydrodynamics equations embedded in STELLA and SNEC codes are quite similar. The principal differences between the codes are in the implementation of radiative transfer into hydrodynamical simulations. STELLA solves implicitly time-dependent equations for the angular moments of intensity in fixed frequency bins which are coupled with the Lagrangian hydrodynamical equations. Therefore, there is no need to ascribe any temperature to the radiation, thus the photon energy distribution may be quite arbitrary. SNEC uses the equilibrium-diffusion approximation for radiation transport. Thus a blackbody spectrum is enforced in SNEC with the same temperature for radiation and matter.

In the SNEC model, the photosphere is located in the outer layers during the first 35 days, and the black-body approximation is quite applicable to the reconstruction of the bolometric light curve. Figure 19 demonstrates a reasonably good agreement of the bolometric fluxes of SNEC and STELLA for this period.

We observe that the two codes agree qualitatively well. The two models can produce the rapid rise of AT2018cow within the first 3 – 4 days. Later the luminosity in STELLA falls a bit faster due to a faster recombination in the outer layers with the mass  $\sim 2 M_{\odot}$  from the edge of the ejecta which are above the photosphere at this epoch. Given many differences in the treatment of opacity and radiative transfer in SNEC and STELLA we find that the agreement is satisfactory. Understanding

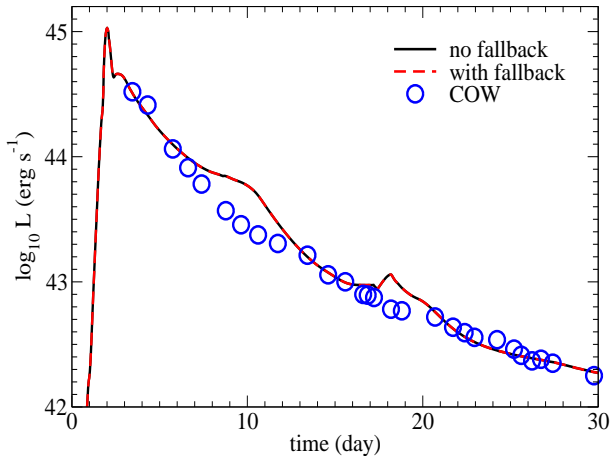


**Figure 20.** Light curve of the comparison model and variations with different CSM composition without or with fallback energy source. The data point corresponds to AT2018cow.

the effect on light curves of different approaches in SNEC and STELLA codes requires a detailed comparative study (Sorokina et al., in preparation).

Note STELLA calculates both the effective temperature  $T_{\text{eff}}$  and the color temperature  $T_{\text{color}}$ . At the shock breakout,  $T_{\text{color}}$  reaches  $\sim 10^6$  K, which is much higher than  $T_{\text{eff}} \sim 10^5$  K obtained by SNEC.

## 6. DISCUSSION

In the previous sections, we have shown that the FBOT-like feature of the early bolometric light curve of AT2018cow is well reproduced by circumstellar interaction in our optimized model before Day 20. After Day 20, the bolometric light curve is well-modeled by radioactive decays, but it requires extensive mixing of  $^{56}\text{Ni}$  almost uniformly up to the ejecta-CSM interface. Thus it is still worth discussing other possible central energy sources to power the late light curve in our PPISN model.

### 6.1. Fallback Onto Black Hole

The progenitor of PPISN is as massive as  $80\text{--}140 M_{\odot}$ , thus it is likely that a black hole is formed in the center. It is possible that fallback of matter onto the black hole occurs to provide a late phase energy source other than the  $^{56}\text{Ni}$  decay or circumstellar interaction. In view of that, we include the fallback energy source in the comparison model. In our spherical explosion model, where we insert an energetic thermal bomb, no direct fallback occurs, so we use a parameterized fallback formula.

We adopt the analytic formula for energy deposition (Michel 1988; Chevalier 1989; Dexter & Kasen 2013)

$$\dot{\epsilon} = A/M_{\text{dep}} t^{-2.5}, \quad (1)$$

where  $A$  is a parameter for the energy deposition rate, and  $M_{\text{dep}}$  is estimated by the photon mean free path. However the compact inner core most of the time leads to energy deposition focused in innermost shells for most of the time.  $A$  is determined by how much mass is accreted during the simulation. The new model has two energy sources: one is the decay of  $^{56}\text{Ni}$  and the other is the fallback.

In Figure 20 we plot the light curves for the two models, and find that the two light curves overlap with each other. This is expected because, in the early light curve, the photosphere is located in CSM or in the outer ejecta. The energy from fallback has indeed modified the internal structure of the core by thermal expansion. However, the timescale for the energy to arrive at the photosphere depends on the diffusion timescale. As a result, no significant change can be seen in the model with the fallback energy deposition.

However, we remark that in multi-dimensional modeling of fallback can be very different from the one-dimensional model. The jet structure may form when the progenitor rotates. The rotating black hole accommodates a rapidly rotating accretion disk, where the gravitational instability in the disk after the formation of dead zone can trigger large-scale mass and energy ejection (see e.g. Tsuruta et al. 2018). In a multi-dimensional model (see, e.g., Tominaga et al. 2007), the jet can break out and form two holes. This drastically reduces the the site of the fallback onto the black hole to the photosphere. To reproduce this phenomenon, we need to parameterize the energy deposition depth into the outer ejecta.

### 6.2. Magnetar Model

We do not consider a magnetar (Kasen & Bildsten 2010; Kasen et al. 2016) as a power source for the late light curve in the present PPISN model because of the following reasons.

- (1) The progenitor of PPISN is so massive as  $80\text{--}140 M_{\odot}$  that it may not form a neutron star remnant.
- (2) Even if we assume the formation of a magnetar in our PPISN model, the diffusion time for the magnetar energy to reach the photosphere would be too long to explain the observed light curve after Day 18, being similar to the black hole accretion model as shown in Figure 20.

Note, however, the magnetar activity may form a jet-like ejecta, The magnetar, which loses energy through its dipole radiation, can effectively transfer its energy by electromagnetic waves along the confined angle. Such a jet-like structure might reduce the timescale to transfer the magnetar energy to the surface.

If the progenitor of AT2018cow would be much smaller star, however, it may not encounter the above two problems (e.g., Fang et al. 2019). In such a low mass model, we need a circumstellar matter to power the early light curve to reproduce the FBOT-like feature. Actually, the super-AGB progenitor of the electron capture supernova forms such CSM as well as a neutron star, and that is the model applied for FBOT, KSN 2015K, by Tolstov et al. (2019). Such a case would be worth investigating for a model of AT2018cow (Sorokina et al. in preparation).

### 6.3. High Energy Photons of AT2018cow

In Margutti et al. (2019) the detailed X-ray and gamma-ray light curve and spectra of AT2018cow are presented.

Here we discuss how the possible energy source of the light curve of AT2018cow (circumstellar interaction, magnetar and accreting BH) can be related to the detected X-ray.

In the circumstellar interaction model, the shock-heated matter has the “color” temperature as high as  $\sim 10^6$  K according to the calculation of STELLA as mentioned in subsection 5.8. Such high temperature materials emit X-rays, which may easily escape from the star.

If the aspherical explosion is the case as illustrated in Figure 12 of Margutti et al. (2019), the ejecta near the “equator” can be ejected faster and is less compact than those near the “poles”. The formation of aspherical circumstellar material allows time-lapse for the interaction to take place.

When bipolar-like explosion takes place, the two poles are more readily to be penetrated by the high velocity flow. Depending on the jet energetics, the jet can breakout directly the surface and trigger the X-ray burst by the interaction.

If the aspherical explosion occurs, the bipolar structure forms as discussed in earlier subsection for the accreting black hole and magnetar, and allows early X-ray emission.

When the shock breakout occurs, it creates an opening of the star reaching directly the compact core. The high-energy photon coming from the black hole or neutron star can escape the star efficiently.

The exact nature of the aspherical explosion and its early high-energy photon emission (see Figure 12 of Margutti et al. (2019)) will require multi-dimensional radiative transfer simulations for understanding, which will be an interesting future project.

## 7. CONCLUSION

In this work we apply the model of circumstellar interaction in the pulsational pair-instability supernova

(PPISN) for explaining the Fast Blue Optical Transient (FBOT) AT2018cow (COW). AT2018cow has quite a unique early light curve, showing a peak as bright as SLSNe but much faster rise and fall than SLSNe. We apply the evolutionary model of the  $42 M_{\odot}$  He star which collapses after undergoing PPI mass ejection, and compute their corresponding bolometric light curves. We have searched for the optimized model parameters (explosion energy, CSM density and structure, and distribution of  $^{56}\text{Ni}$ ) with which the bolometric light curve of AT2018cow is well-reproduced.

We show that an explosion of PPISN with the energy  $\sim 5 \times 10^{51}$  erg, a  $^{56}\text{Ni}$  mass of  $\sim 0.6 M_{\odot}$ , CSM mass of  $0.5 M_{\odot}$  and a density of  $10^{-11}$  g cm $^{-3}$  produce an optimized model whose bolometric light curve is in best agreement with AT2018cow.

We also studied how each model parameter affects the light curve. We note that the simulation reaches the convergence regime in the resolution (mass shell  $\sim 2 \times 10^{31}$  g). The explosion energy plays a secondary role in the light curve shape. On the other hand, the CSM mass, density, and the structure dominate the light curve shape. Mixing of  $^{56}\text{Ni}$  is necessary to explain the slow decline of the luminosity beyond Day 20. Observable differences in the photosphere evolution suggests that further validations are necessary to connect the FBOT AT2018cow to PPISN model.

To explain the late time light curve and the high-energy photon after shock breakout, a central engine such as fallback onto a black hole or a magnetar remains important. Despite that, the interaction can still provide the necessary condition for the rapid rise and drop of the light curve up to  $\sim 40$  days. Further discrimination of models will require multi-dimensional simulations to trace how the aspherical energy deposition contributes to the high energy photons detected.

Based on our successful model for FBOT (AT2018cow) with the CSM mass of  $0.5 M_{\odot}$  and the model for SLSN (Tolstov et al. 2017) with the CSM mass of ( $\sim 20 M_{\odot}$ ), we set the following working hypothesis that PPISN produces SLSNe if CSM is massive enough and FBOTs if CSM is less than  $\sim 1 M_{\odot}$ .

## 8. ACKNOWLEDGMENT

This work was supported by World Premier International Research Center Initiative (WPI Initiative), MEXT, Japan, and JSPS KAKENHI Grant Number JP17K05382 and JP20K04024. K.N. would like to thank Brian Metzger and Raffaella Margutti for useful discussion at the UCSB/KITP workshop “The New Era of Gravitational-Wave Physics and Astrophysics” in 2019. S.C.L thank the MESA development commu-

nity for making the code open-sourced and V. Morozova and her collaborators in providing the SNEC code open source. S.C.L. acknowledges support by funding HST-AR-15021.001-A and 80NSSC18K1017. S.B. is sponsored by grant RSF 19-12-00229 in his work on the su-

pernova simulations with STELLA code. P.B.'s work on understanding the effect on light curves of different approaches in SNEC and STELLA codes is supported by the grant RSF 18-12-00522. E.S. is supported by the grant RFBR 19-52-50014 in her work on developing codes modeling the radiative transfer in SNe.

## REFERENCES

- Baklanov, P. V., Sorokina, E. I., & Blinnikov, S. I. 2015, *Astronomy Letters*, 41, 95, doi: [10.1134/S1063773715040027](https://doi.org/10.1134/S1063773715040027)
- Barkat, Z., Rakavy, G., & Sack, N. 1967, *PhRvL*, 18, 379, doi: [10.1103/PhysRevLett.18.379](https://doi.org/10.1103/PhysRevLett.18.379)
- Bietenholz, M. F., Margutti, R., Coppejans, D., et al. 2020, *MNRAS*, 491, 4735, doi: [10.1093/mnras/stz3249](https://doi.org/10.1093/mnras/stz3249)
- Blinnikov, S. I., Röpke, F. K., Sorokina, E. I., et al. 2006, *A&A*, 453, 229, doi: [10.1051/0004-6361:20054594](https://doi.org/10.1051/0004-6361:20054594)
- Chatzopoulos, E., & Wheeler, J. C. 2012, *Astrophys. J.*, 748, 42
- Chevalier, R. A. 1989, *ApJ*, 346, 847, doi: [10.1086/168066](https://doi.org/10.1086/168066)
- Dexter, J., & Kasen, D. 2013, *ApJ*, 772, 30, doi: [10.1088/0004-637X/772/1/30](https://doi.org/10.1088/0004-637X/772/1/30)
- Fang, K., Metzger, B. D., Murase, K., Bartos, I., & Kotera, K. 2019, *ApJ*, 878, 34, doi: [10.3847/1538-4357/ab1b72](https://doi.org/10.3847/1538-4357/ab1b72)
- Fox, O. D., & Smith, N. 2019, *MNRAS*, 488, 3772, doi: [10.1093/mnras/stz1925](https://doi.org/10.1093/mnras/stz1925)
- Gal-Yam, A. 2012, *Science*, 337, 927, doi: [10.1126/science.1203601](https://doi.org/10.1126/science.1203601)
- Goicovic, F. G., Springel, V., Ohlmann, S. T., & Pakmor, R. 2019, *MNRAS*, 487, 981, doi: [10.1093/mnras/stz1368](https://doi.org/10.1093/mnras/stz1368)
- Heger, A., & Woosley, S. E. 2002, *Astrophys. J.*, 567, 532
- Iglesias, C. A., & Rogers, F. J. 1993, *ApJ*, 412, 752, doi: [10.1086/172958](https://doi.org/10.1086/172958)
- . 1996, *ApJ*, 464, 943, doi: [10.1086/177381](https://doi.org/10.1086/177381)
- Kasen, D., & Bildsten, L. 2010, *ApJ*, 717, 245, doi: [10.1088/0004-637X/717/1/245](https://doi.org/10.1088/0004-637X/717/1/245)
- Kasen, D., Metzger, B. D., & Bildsten, L. 2016, *ApJ*, 821, 36, doi: [10.3847/0004-637X/821/1/36](https://doi.org/10.3847/0004-637X/821/1/36)
- Kuin, N. P. M., Wu, K., Oates, S., et al. 2019, *MNRAS*, 487, 2505, doi: [10.1093/mnras/stz053](https://doi.org/10.1093/mnras/stz053)
- Kumagai, S., Shigeyama, T., Nomoto, K., et al. 1989, *ApJ*, 345, 412, doi: [10.1086/167915](https://doi.org/10.1086/167915)
- Leung, S.-C., Nomoto, K., & Blinnikov, S. 2019, *ApJ*, 887, 72, doi: [10.3847/1538-4357/ab4fe5](https://doi.org/10.3847/1538-4357/ab4fe5)
- Leung, S.-C., Nomoto, K., & Suzuki, T. 2020, *ApJ*, 889, 34, doi: [10.3847/1538-4357/ab5d2f](https://doi.org/10.3847/1538-4357/ab5d2f)
- Liu, L.-D., Zhang, B., Wang, L.-J., & Dai, Z.-G. 2018, *ApJL*, 868, L24, doi: [10.3847/2041-8213/aaeff6](https://doi.org/10.3847/2041-8213/aaeff6)
- Lyutikov, M., & Toonen, S. 2019, *MNRAS*, 487, 5618, doi: [10.1093/mnras/stz1640](https://doi.org/10.1093/mnras/stz1640)
- Marchant, P., Renzo, M., Farmer, R., et al. 2019, *ApJ*, 882, 36, doi: [10.3847/1538-4357/ab3426](https://doi.org/10.3847/1538-4357/ab3426)
- Margutti, R., Metzger, B. D., Chornock, R., et al. 2019, *ApJ*, 872, 18, doi: [10.3847/1538-4357/aafa01](https://doi.org/10.3847/1538-4357/aafa01)
- Michel, F. C. 1988, *Nature*, 333, 644, doi: [10.1038/333644a0](https://doi.org/10.1038/333644a0)
- Morozova, V., Piro, A. L., Renzo, M., et al. 2015, *ApJ*, 814, 63, doi: [10.1088/0004-637X/814/1/63](https://doi.org/10.1088/0004-637X/814/1/63)
- Nomoto, K. 1984, *ApJ*, 277, 791, doi: [10.1086/161749](https://doi.org/10.1086/161749)
- Nomoto, K., & Kondo, Y. 1991, *ApJL*, 367, L19, doi: [10.1086/185922](https://doi.org/10.1086/185922)
- Ohkubo, T., Nomoto, K., Umeda, H., Yoshida, N., & Tsuruta, S. 2009, *ApJ*, 706, 1184, doi: [10.1088/0004-637X/706/2/1184](https://doi.org/10.1088/0004-637X/706/2/1184)
- Paczynski, B. 1983, *ApJ*, 267, 315, doi: [10.1086/160870](https://doi.org/10.1086/160870)
- Paxton, B., Bildsten, L., Dotter, A., et al. 2011, *Astrophys. J. Suppl.*, 192, 3
- Paxton, B., Cantiello, M., Arras, P., et al. 2013, *Astrophys. J. Suppl.*, 208, 4
- Paxton, B., Marchant, P., Schwab, J., et al. 2015, *Astrophys. J. Suppl.*, 220, 15
- Paxton, B., Schwab, J., Bauer, E. V., et al. 2017, *Astrophys. J. Suppl.*, 234, 34
- Perley, D. A., Mazzali, P. A., Yan, L., et al. 2019, *MNRAS*, 484, 1031, doi: [10.1093/mnras/sty3420](https://doi.org/10.1093/mnras/sty3420)
- Prentice, S. J., Maguire, K., Smartt, S. J., et al. 2018, *ApJL*, 865, L3, doi: [10.3847/2041-8213/aadd90](https://doi.org/10.3847/2041-8213/aadd90)
- Rest, A., Garnavich, P., Khatami, D., et al. 2018, in *American Astronomical Society Meeting Abstracts*, Vol. 231, American Astronomical Society Meeting Abstracts #231, 446.06
- Sorokina, E., Blinnikov, S., Nomoto, K., Quimby, R., & Tolstov, A. 2016, *ApJ*, 829, 17, doi: [10.3847/0004-637X/829/1/17](https://doi.org/10.3847/0004-637X/829/1/17)
- Tanikawa, A. 2018a, *ApJ*, 858, 26, doi: [10.3847/1538-4357/aaba79](https://doi.org/10.3847/1538-4357/aaba79)
- . 2018b, *MNRAS*, 475, L67, doi: [10.1093/mnrasl/sly006](https://doi.org/10.1093/mnrasl/sly006)
- Tolstov, A., Nomoto, K., Blinnikov, S., et al. 2017, *Astrophys. J.*, 835, 266

- Tolstov, A., Nomoto, K., Sorokina, E., et al. 2019, *ApJ*, 881, 35, doi: [10.3847/1538-4357/ab2876](https://doi.org/10.3847/1538-4357/ab2876)
- Tominaga, N., Umeda, H., & Nomoto, K. 2007, *ApJ*, 660, 516, doi: [10.1086/513063](https://doi.org/10.1086/513063)
- Tsuruta, S., Leung, S.-C., & Nomoto, K. 2018, *International Journal of Modern Physics D*, 27, 1830004, doi: [10.1142/S0218271818300045](https://doi.org/10.1142/S0218271818300045)
- Woosley, S. E. 2017, *Astrophys. J.*, 836, 244
- Woosley, S. E., Blinnikov, S., & Heger, A. 2007, *Nature*, 450, 390
- Yoshida, T., Okita, S., & Umeda, H. 2014, *MNRAS*, 438, 3119, doi: [10.1093/mnras/stt2427](https://doi.org/10.1093/mnras/stt2427)
- Zha, S., Leung, S.-C., Suzuki, T., & Nomoto, K. 2019, *ApJ*, 886, 22, doi: [10.3847/1538-4357/ab4b4b](https://doi.org/10.3847/1538-4357/ab4b4b)